



Inferring spatial source of disease outbreaks using maximum entropyMehrad Ansari ¹, David Soriano-Paños,^{2,3} Gourab Ghoshal,⁴ and Andrew D. White ^{1,*}¹*Department of Chemical Engineering, University of Rochester, Rochester, New York 14627, USA*²*Instituto Gulbenkian de Ciência (IGC), Oeiras 2780-156, Portugal*³*GOTHAM Lab, Institute for Biocomputation and Physics of Complex Systems, University of Zaragoza, E-50009 Zaragoza, Spain*⁴*Department of Physics and Astronomy and Computer Science, University of Rochester, Rochester, New York 14627, USA*

(Received 15 October 2021; revised 9 February 2022; accepted 29 June 2022; published 21 July 2022)

Mathematical modeling of disease outbreaks can infer the future trajectory of an epidemic, allowing for making more informed policy decisions. Another task is inferring the origin of a disease, which is relatively difficult with current mathematical models. Such frameworks, across varying levels of complexity, are typically sensitive to input data on epidemic parameters, case counts, and mortality rates, which are generally noisy and incomplete. To alleviate these limitations, we propose a maximum entropy framework that fits epidemiological models, provides calibrated infection origin probabilities, and is robust to noise due to a prior belief model. Maximum entropy is agnostic to the parameters or model structure used and allows for flexible use when faced with sparse data conditions and incomplete knowledge in the dynamical phase of disease-spread, providing for more reliable modeling at early stages of outbreaks. We evaluate the performance of our model by predicting future disease trajectories based on simulated epidemiological data in synthetic graph networks and the real mobility network of New York State. In addition, unlike existing approaches, we demonstrate that the method can be used to infer the origin of the outbreak with accurate confidence. Indeed, despite the prevalent belief on the feasibility of contact-tracing being limited to the initial stages of an outbreak, we report the possibility of reconstructing early disease dynamics, including the epidemic seed, at advanced stages.

DOI: [10.1103/PhysRevE.106.014306](https://doi.org/10.1103/PhysRevE.106.014306)**I. INTRODUCTION**

The spread of SARS-CoV-2 virus constitutes the most recent example of the vulnerability of modern society to the spread of communicable diseases [1–3]. In particular, the combination of features such as extensive trans- and intranational transportation networks, shortening travel time between faraway regions [4–6], the existence of important socioeconomic inequities [7–9], and the phenomenon of rapid urbanization [10,11] have conspired to give rise to the unprecedented speed at which SARS-CoV-2 has advanced, becoming a global threat within a few months of the (reported) initial outbreak.

The initial stages of disease spread of novel pathogens are critical because of the lack of knowledge of disease characteristics and lack of therapeutics or vaccines. Indeed, early attempts at mitigation resorted to nonpharmaceutical interventions such as recommending hand-washing, hygienic measures, social distancing, travel restrictions, and population confinement via stay-at-home orders [12–14]. A key tool for

devising and assessing the effectiveness of such measures is mathematical modeling of the epidemic trajectories under various scenarios. The advantage of such models are twofold: On the one hand, epidemic models provide short-term forecasts on the evolution of an outbreak, providing useful information to assess the potential harmfulness of the pathogen and act accordingly to reduce their impact. On the other hand, the different layers of complexity introduced in the epidemic models has boosted their use as benchmarks to devise cost-effective nonpharmaceutical interventions aimed at hindering the spread of the disease [15,16].

Regardless of their stochastic or deterministic nature [17–19], the successful application of epidemic models to provide reliable forecasts is tightly linked with the correct estimation of their relevant parameters. Early in an epidemic, the key parameters describing the spread of the infection are highly uncertain, and this uncertainty can severely impact the predicted outcomes [20]. This becomes particularly relevant in the context of highly complex compartmental models that produce wildly varying degenerate trajectories in the short-term dynamics, even for small changes in the parameter estimates [21,22]. While this degeneracy dissipates in the long-term dynamics due to exponential growth encoded in the equations, even minor inaccuracies in the epidemic parameters limits reliable predictions to at most a few weeks in the future [23]. Given this, the practical efficacy of epidemiological models is in providing a range of possible outcomes rather than producing precise quantitative predictions [24].

*andrew.white@rochester.edu

Published by the American Physical Society under the terms of the [Creative Commons Attribution 4.0 International](https://creativecommons.org/licenses/by/4.0/) license. Further distribution of this work must maintain attribution to the author(s) and the published article's title, journal citation, and DOI.

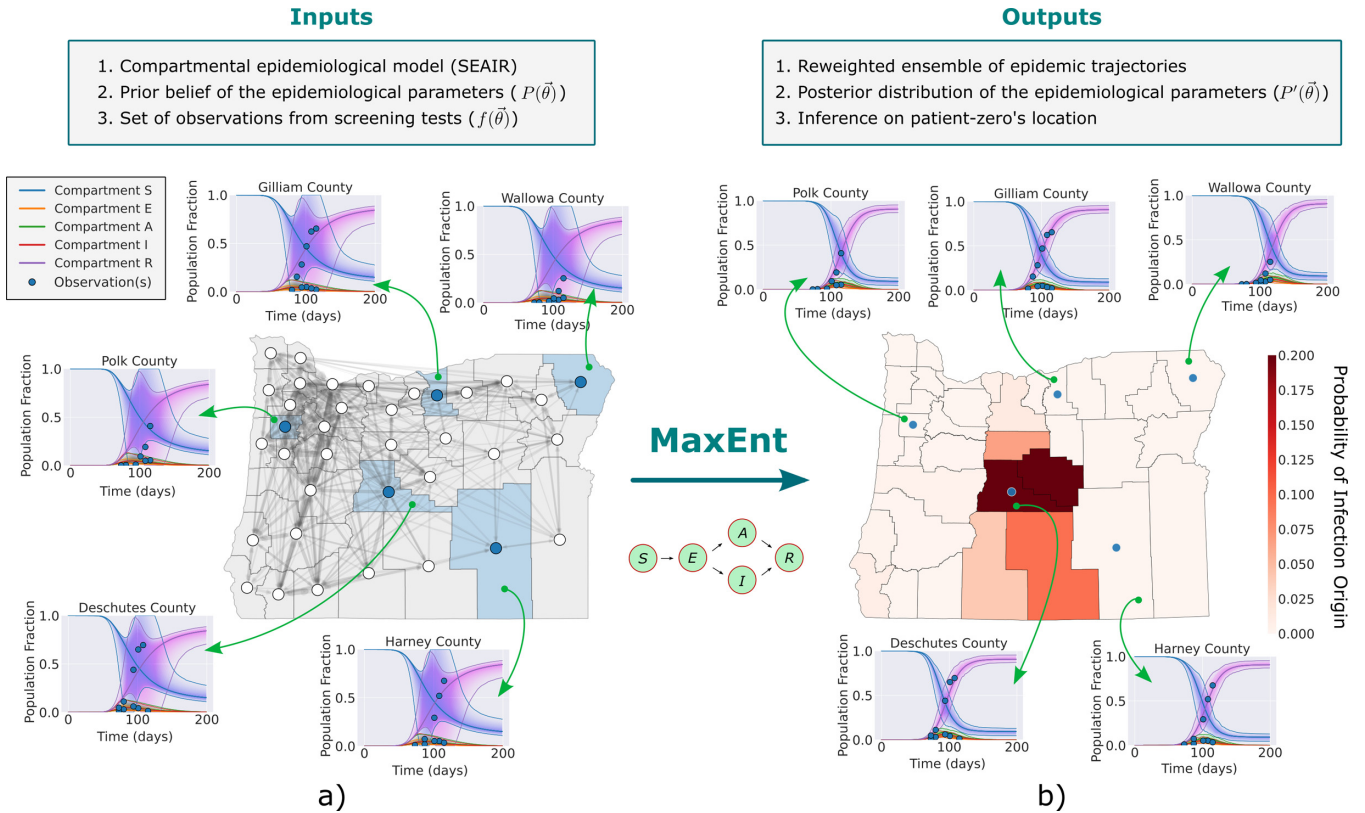


FIG. 1. High-level model overview. (a) Model inputs: an SEAIR compartmental epidemiological model, prior belief of the epidemiological parameters, and a set of sparse observations that come from disease screening tests. The contact network in a metapopulation can be represented as a network graph. The infection starts at an unknown origin and spreads through the network. We generate a large set of trajectories and explore the epidemic trajectory space over a high variance prior belief for the epidemiology parameters. The large variance is represented as the shaded areas with 80% confidence intervals. The infection starts in a single node in each trajectory series, but that node varies over the next trajectories. (b) Model outputs: MaxEnt reweighted ensemble of trajectories given the observations, posterior distributions of the parameters, and predicted infection origin. The reweighted trajectories allow us to predict how the disease spreads through the network and infer the location for the source of infection.

Multiple ways to infer epidemiological parameters have been proposed in the literature. One typical method is to use maximum likelihood approaches, where parameter values are chosen to maximize the likelihood of observing the experimentally measured data (observations), given some prior distribution of the parameters [25,26]. A disadvantage of this method is that the functional form of the likelihood function must be known or approximated to perform maximization. Another approach is least-squares fitting, which employs various optimization methods, including but not limited to Markov-chain Monte Carlo [27–30], sequential Monte Carlo [31–33], trajectory matching [34–38], and machine learning methods such as support vector machines [39]. Other approaches include generalized profiling [40], approximate Bayesian computation [41–43], derivative-free optimization [44,45], and Bayesian inference [46–50]. Furthermore, most of the epidemiological models in the literature focus on forward dynamics of the diffusion of the pathogen through the network, while the backward-dynamics problem of identifying the diffusion source has been comparatively less studied [51–53]. Such an analysis bears significant importance in guiding systematic contact-tracing and increasing the chance of early containment of an outbreak.

An approach that circumvents these difficulties is a well-known method from statistical mechanics, maximum entropy (MaxEnt) biasing. MaxEnt has been proven to be successful in various settings such as molecular dynamics simulations [54–56], ecology [57–60], nuclear magnetic resonance spectroscopy [61,62], x-ray diffraction [63,64], electron microscopy [65,66], economics [67], and neuroscience [68–71]. This method uses the principle of entropy to measure the difference between two distributions or trajectories and applies a change using Lagrange multipliers to alter a given distribution to match a target one, while maximizing the entropy (and thus, effecting minimal change) [72]. Unlike the inference methods mentioned earlier, where the main goal is to estimate the model’s parameters, MaxEnt aims at reweighting an ensemble of trajectories generated by the model, such that their corresponding average fits a set of sparse observed data. This approach is highly promising in the context of epidemic modeling, as it mitigates the need for designing complex compartmental models and having to make a lot of simplifying assumptions. As remarked in Ref. [73]: “What has been produced the day before often must be completely revised the day after because a new piece of information has arrived.” This approach relies more on daily (weekly)

evidence rather than relying on uncertain early estimates of disease parameters, especially at the early stages of an epidemic outbreak. A few instances of applying MaxEnt to characterize epidemic spreading exist in the literature. Law *et al.* [74] provided an analysis for spatiotemporal spread of syphilis. However, their analysis relied not on transient dynamics governed by compartmental models but rather on a time-dependent covariance matrix constructed based on the spatial distribution measurements of confirmed cases across different areas over several years. In Ref. [75], MaxEnt is used to bias the epidemic curves generated by mean-field SIS (Susceptible, Infectious, Susceptible) and SIR (Susceptible, Infectious, Recovered) compartmental models to reproduce a set of empirical observations and uncover probability distributions used for contagion and recovery events. Harding *et al.* [76] propose a MaxEnt approach to modify a SIS framework running on a contact network to model the time-varying nature of human mobility in response to the diffusion of an epidemic outbreak.

Here we explore the use of MaxEnt biasing when more layers of complexity are added to the dynamic equations governing the advance of an epidemic. To do so, we consider a more elaborated compartmental scheme, the SEAIR model, running on metapopulations [77,78] to accommodate different realistic features such as human mobility, the relevance of the incubation period of one pathogen, or the existence of asymptomatic infectious individuals [1]. The novelty of our approach lies in inferring *disease trajectories* directly rather than model parameters. This enables simultaneous estimation of disease progression before (backward dynamics) and after (forward dynamics) the observations. We show that making the objective to fit the ensemble of trajectories, rather than directly inferring model parameters, enables accurate identification of the spatial source of infection and how the infection spreads across the metapopulation, even with sparse observations.

In Fig. 1, we represent a high-level overview of the framework. Graphs in this work were generated using NetworkX [79]. Model inputs include a compartmental epidemiology model, prior belief for its parameters, and a set of sparse observations. The prior belief on the model parameters can include a relatively large variance, making our approach highly applicable to risk assessment analysis at the early stages of the outbreak, where the true parameters are unknown. The observations are weekly average data obtained by disease test screenings that contain random noise. This noise accounts for the uncertainty associated with the number of infected individuals due to the variance of testing policies across a metapopulation. The output is the MaxEnt reweighted trajectories that are used for inference on the epidemic spread and the source of infection.

All the results in this work are benchmarked against data obtained from epidemiological simulations with preselected parameters. This data is referred to as the *ground-truth* model onwards. The term “ground truth” means data that are known to be true and are what the inference method should match. This convention is from statistical inference. The definition of the *ground-truth* model allows us to benchmark and access the prediction performance of our approach in inferring disease dynamics without ethical and practical concerns. Note that

ground truth does not mean data obtained from real-world empirical measurements; however, we apply a few settings under which our approach can have a stronger connection with the real-world epidemiological data: (1) The values for the preselected epidemiological parameters used for generating the *ground-truth* models are within ranges similar to other real-world disease pathogens and (2) the sampled disease trajectories share the same demographic distributions as the *ground-truth* model. However, as they are generated based on a large variance prior belief on the epidemiological parameters and variations of the mobility flows, they do not represent the exact correct dynamics as the ones in the *ground-truth* model. This allows us to replicate the similar situation of lacking precise knowledge about the disease pathogen at the early stages of an outbreak in a real-world scenario. (3) Inference is done based on sparse noisy observations obtained from {I, R} compartments only. Considering a real-world setting, collecting data from these two compartments is more practical than others. (4) By allowing for some disagreement between the MaxEnt reweighted fit and noisy observations, we are replicating the common case of under-reporting in real-world epidemiological data.

The manuscript is organized as follows. In Sec. II A, we describe the theory of MaxEnt applied to a general model function and describe the procedure for MaxEnt path biasing. In Sec. II B we describe the underlying equations of the SEAIR model occurring on a metapopulation framework. In Sec. III we present results on both synthetic and real-world metapopulation mobility networks, demonstrate how the method can predict infection spread, and make a high certainty inference on the source of an epidemic using the posterior reweighted trajectory from the MaxEnt approach. In particular, we demonstrate that this inference can be done even in late stages of the disease dynamics. In Sec. IV we end with a discussion of the implications of our findings.

II. THEORY

A. Maximum entropy with uncertainty

The principle of maximum entropy is founded based on the probabilistic definition of entropy, a measure of the spread of a probability distribution. The goal is to infer a probability distribution with the largest uncertainty (i.e., maximum entropy) subject to a set of observations (constraints). The power of this approach lies in its ability to reduce the model order by inferring the state of underconstrained dynamical systems, where the number of unknowns exceeds the number of equations.

Consider that for a given simulator $f(\vec{\theta})$ with a set of parameters $\vec{\theta}$, we have a prior distribution of parameters $\mathcal{P}(\vec{\theta})$. For example, the function $f(\vec{\theta})$ can be a system of ODEs in a compartmental epidemiology model. Suppose we have a set of N observations g_k with uncertainty ϵ_k , where $k \in [1, \dots, N]$. We constrain our prior model $\mathcal{P}(\vec{\theta})$ to observations such that:

$$\int d\vec{\theta} d\vec{\epsilon} \mathcal{P}'(\vec{\theta}) \mathcal{P}_0(\epsilon_k) \{g_k[f(\vec{\theta})] + \epsilon_k\} = E[g_k + \epsilon_k] = \bar{g}_k \quad \forall k. \quad (1)$$

This means that we want the average over the posterior distribution $\mathcal{P}'(\vec{\theta})$ to match the observation data with some

allowable disagreement based on $\{\epsilon_k\}$. The expected value of the observations given their corresponding allowable disagreements of $\mathcal{P}_0(\epsilon)$ based on $\{\epsilon_k\}$ are denoted with $\{\bar{g}_k\}$ in Eq. (1). Note that unlike in Bayesian frameworks, the mentioned average disagreement with the data is optional. In case of a perfect match with data, the error distribution is set to a Dirac δ about 0 [i.e., $\mathcal{P}_0(\epsilon_k) = \delta(\epsilon_k = 0)$]. However, in our settings, the Laplace distribution prior $\mathcal{P}_0(\epsilon)$ is used to account for some disagreement with a given standard deviation σ_0 , thus:

$$\mathcal{P}_0(\epsilon) = -\frac{\epsilon\sigma_0^2}{1 - \frac{\epsilon^2\sigma_0^2}{2}}. \quad (2)$$

This definition does not describe the underlying variance of the observational data but rather it is a means of accounting for the epistemic uncertainty and underreporting that comes with disease test screening data measurements as an average bias in agreement. The posterior distribution $\mathcal{P}'(\theta)$ that satisfies N constraints is given by [56,80–82]:

$$\mathcal{P}'(\bar{\theta}, \bar{\epsilon}) = \frac{1}{Z'} \mathcal{P}(\bar{\theta}) \prod_k^N e^{-\lambda_k g_k [f(\bar{\theta})]} e^{-\lambda_k \epsilon_k} \mathcal{P}_0(\epsilon_k), \quad (3)$$

$$Z' = \int d\bar{\theta} d\bar{\epsilon} \mathcal{P}(\bar{\theta}) \mathcal{P}_0(\epsilon) e^{-\sum_k \lambda_k [g_k [f(\bar{\theta})] + \epsilon_k]}, \quad (4)$$

where Z' is a normalization constant and λ_k values are iteratively updated using gradient descent to satisfy the constraint $E[g_k + \epsilon_k] = \bar{g}_k$. More information on the MaxEnt model implemented in this study can be found in the work of Barrett *et al.* [72].

Using this method applies minimal change to the model's original output, without altering the parameters directly. The premise of this change is that the original model is treated as well trusted but only slightly incorrect, with the intent of improving predictive accuracy for future events by matching the model's output to experimental data (observations). However, experimental data are known to contain systematic error, so we include a formulation of MaxEnt that accounts for some bias.

The MaxEnt framework suggests a strong belief in our prior distribution of parameters, which reflects the use of *approximately correct* parameters. In this setting, the term *approximately correct* suggests that the prior distribution of model's parameters are not chosen at random but rather with epidemiological intuitions. Even in cases where little to no information is available on novel pathogens, the magnitude of general epidemiological parameters that describe how the infection spreads are bounded within certain values. These bounded limits can be used as an initial guess for the mentioned prior distribution. In the case of epidemics, the outcome of MaxEnt algorithm is an ensemble of weighted epidemic trajectories, whose average reproduces the observed data with some allowable disagreement. In this setting, the observations can be the number of confirmed disease cases, given some random noise to account for uncertainty.

This method is agnostic to the functional form of the original model; given that it reweights paths produced by sampling model parameters, which can be done *a priori*, it can be treated as a black box. This also has the advantage that the method's computational complexity scales with only the number of

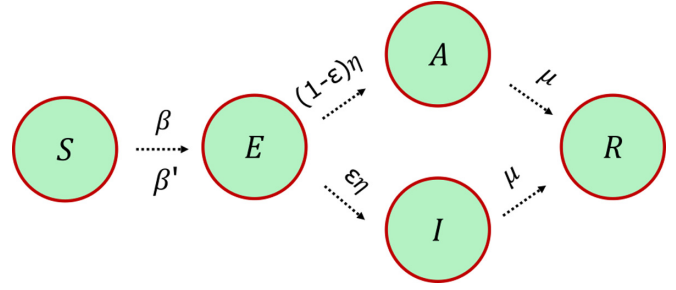


FIG. 2. SEAIR compartmental scheme. Populations in each patch can be any of susceptible, exposed, asymptomatic, infected, and resolved. Susceptible (S) individuals can get exposed (E) to the disease through I-S and A-S interactions, with probability per contact β and β' , respectively. Once exposed, they become asymptomatic (A) or infected (I) with probabilities $(1 - \epsilon)\eta$ and $\epsilon\eta$. They finally recover or die with probability μ and become resolved (R). Note that η and μ are related to the latent period and the infectious window, respectively, whereas ϵ accounts for the fraction of infected (symptomatic) individuals.

paths sampled and number of target functions rather than the number of model parameters [72].

B. Epidemic model

Epidemic spreading can be represented as a reaction-diffusion process, where the reaction term refers to the contagion events triggered by the interaction between infected and susceptible hosts whereas the diffusion phase corresponds to the spatial dissemination of the population across the system under study. In this sense, metapopulations, originally introduced in the field of ecology, represent a convenient framework, balancing complexity with analytical tractability, to account for the impact of mobility on epidemic spreading [83–85]. Metapopulations are composed of spatial patches (nodes) where local populations interact in a mean-field manner, connected via flows (edges) corresponding to movement of individuals between patches. The spatial resolution of the spatial patch may vary (neighborhoods, zip codes, districts, cities, etc.) depending on the granularity of the input data or the scale at which the dynamics are being modeled. In what is to follow, we assume that our metapopulation is composed of N_p patches and that each patch i is populated by n_i residents.

To model the disease spread, we consider a discrete-time variant of the Susceptible-Exposed-Infected-Removed (SEIR) model to account for the existence of (A)symptomatic individuals. With the addition of compartment A, our model is denoted as the SEAIR model. The choice for this particular flavor of compartments was inspired by its relevance in modeling the evolution of the current COVID-19 pandemic [86,87]. The schematic of the model is detailed in Fig. 2. At each time step, susceptible individuals (S) become exposed (E) by interacting with asymptomatic (A) and infectious (I) agents with probability Π . This probability depends on the probability of infection per every I-S and A-S contact, denoted with β and β' , respectively. Exposed individuals turn into asymptomatic or symptomatic infected with a probability η , distributing between both compartments as dictated by fraction of symptomatic individuals denoted by ϵ . Finally, μ

denotes the probability that an asymptomatic or symptomatic individual recovers or dies, thus becoming resolved (R). Once resolved, the individuals have lifelong immunity and can no longer be infected. Note that the probabilities η and μ can be related to the latent period and the infectious window included in continuous-time approaches [88].

Considering mobility, we follow the movement-interaction-return scheme introduced in Ref. [89] to reflect the impact of commuting mobility on epidemic spreading. At the movement stage, the individuals are redistributed across the network according to the flows encoded in the links of the metapopulation. Following the redistribution of the population, contagion and recovery processes take place at the interaction stage, changing the epidemic state of the population accordingly. Finally, to reflect the recurrent nature of daily human movements, all the agents come back to their associated residential areas. All the equations in this work are formulated based on an uncontrolled scenario, where there are no restrictions imposed on the mobility patterns of the metapopulation.

The spreading process is represented through a temporally discretized ODE that includes the spatial distribution of the population as well as their mobility patterns [90]. Here we aim at characterizing the evolution of the fraction of agents in state m (where $m \in \{S, E, A, I, R\}$) associated with each node i , denoted in the following by $\rho_i^m(t)$. The temporal evolution of these quantities are given by:

$$\rho_i^S(t+1) = [1 - \Pi_i(t)]\rho_i^S(t), \quad (5)$$

$$\rho_i^E(t+1) = (1 - \eta)\rho_i^E(t) + \rho_i^S(t)\Pi_i(t), \quad (6)$$

$$\rho_i^A(t+1) = (1 - \epsilon)\eta\rho_i^E(t) + (1 - \mu)\rho_i^A(t), \quad (7)$$

$$\rho_i^I(t+1) = \epsilon\eta\rho_i^E(t) + (1 - \mu)\rho_i^I(t), \quad (8)$$

$$\rho_i^R(t+1) = \rho_i^R(t) + \mu[\rho_i^I(t) + \rho_i^A(t)]. \quad (9)$$

$\Pi_i(t)$ denotes the probability that a susceptible agent associated with node i contracts the disease by making contacts with an asymptomatic or infected individual. Under our assumptions regarding human mobility, it can be expressed as:

$$\Pi_i(t) = \sum_{j=1}^{N_p} R_{ij}P_j(t), \quad (10)$$

where R_{ij} represents the probability of a resident inside patch i moving to patch j , and $P_j(t)$ is the probability of contracting the disease inside node j at time t . Assuming that the number of trips recorded between both locations in a real dataset is given by the origin-destination (OD) matrix T_{ij} , the elements of the mobility matrix R are easily computed as $R_{ij} = T_{ij} / \sum_j T_{ij}$. Thus, under the well-mixed assumption, $P_i(t)$ becomes

$$P_i(t) = 1 - \prod_{j=1}^{N_p} (1 - \beta) z_f \left(\frac{n_j^{\text{eff}}}{a_i} \right)^{\frac{n_{j \rightarrow i}^I(t)}{n_i^{\text{eff}}}} (1 - \beta') z_f \left(\frac{n_j^{\text{eff}}}{a_i} \right)^{\frac{n_{j \rightarrow i}^A(t)}{n_i^{\text{eff}}}}. \quad (11)$$

Note that the product term in Eq. (11) accounts for the probability for an individual not getting infected while staying in node i and the exponent represents the number of contacts made with the infectious individuals from compartments A and I. To compute these contacts, we assume that the number of interactions increases monotonically with the population density in each patch according to a function f , given by

$$f(n_i^{\text{eff}}) = 2 - e^{-\xi n_i^{\text{eff}}/a_i}. \quad (12)$$

where ξ is a constant ($\xi = 5 \times 10^{-3}$ square miles throughout the whole manuscript), a_i corresponds to the area of patch i and n_i^{eff} represents the effective population gathered inside patch i after the movement stage. Taking into account the mobility matrix, the latter is given by:

$$n_i^{\text{eff}} = \sum_{j=1}^{N_p} R_{ji}n_j. \quad (13)$$

For every contact, each individual interacts with another at random. Therefore, the probability of interaction with an infectious individual belonging to the compartment m at time t inside patch i is given by $n_{j \rightarrow i}^m(t)/n_i^{\text{eff}}$, where $n_{j \rightarrow i}^m$ is the number of infectious agents going from j to i belonging to the compartment m , and a_i denotes the area of node i . In particular:

$$n_{j \rightarrow i}^A(t) = R_{ji}n_j\rho_j^A(t), \quad (14)$$

$$n_{j \rightarrow i}^I(t) = R_{ji}n_j\rho_j^I(t). \quad (15)$$

Finally, z is a normalization function to ensure that the average number of contacts across the whole population is $\langle k \rangle$. Therefore,

$$z = \frac{N^{\text{TOT}} \langle k \rangle}{\sum_{i=1}^{N_p} n_i^{\text{eff}} f\left(\frac{n_i^{\text{eff}}}{a_i}\right)}, \quad (16)$$

where N^{TOT} is the total number of individuals across the metapopulation, i.e., $N^{\text{TOT}} = \sum_{j=1}^{N_p} n_j$.

III. RESULTS

In what it is to follow, with an initial guess on the epidemiological parameters and a set of observations, we apply our method to address two fundamental problems in epidemiology modeling: (1) Early assessment of the potential spread and (2) identifying the origin of the outbreak. For observations, we consider weekly averages for the fraction of the population in compartments I and R. We choose these two compartments, given that these are the most likely for which somewhat reliable estimates can be made from real-world data. Nevertheless, it is well documented [91] that such estimates are noisy and their fidelity varies from region to region. To account for some degree of uncertainty about the data, we add multiplicative noise with a mean 1 and standard deviation 0.05 to the observations obtained from the *ground-truth* trajectory. The sampling process tries to explore the trajectory space by adjusting the epidemiological parameters such as β , β' , ϵ , η , and μ from normal or truncated normal distributions, while

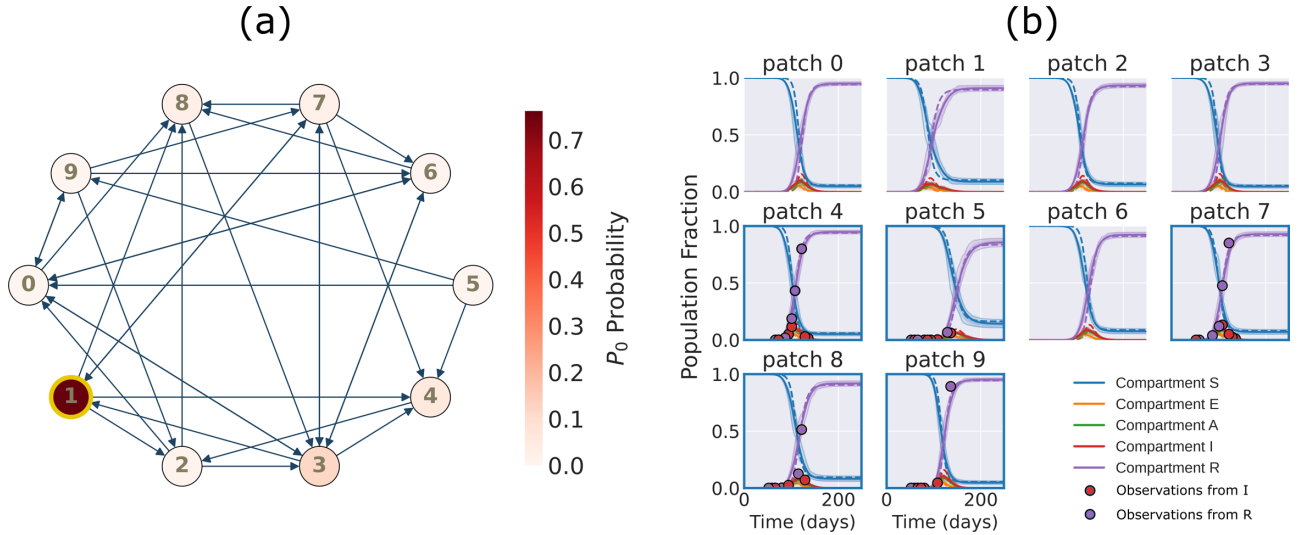


FIG. 3. Predicting forward and backward dynamics in a synthetic contact network. (a) A sparse synthetic metapopulation network with $N_p = 10$ and edge-connection probability $\tau = 0.4$. Nodes indicate spatial regions (containing a fully mixed population) and directed edges represent mobility flows. The ground-truth model is generated by seeding the infection in a single individual residing in Node 1 (highlighted in yellow) at time $t = 0$. Each node is colored according to their P_0 probabilities (the probability of being the source of infection) as calculated by the model. The model predicts that node 1 is the most probable source with 76% certainty. (b) Dashed curves represent the *ground-truth* trajectories in each patch for the SEAIR model over a period of 250 days (each time-unit t is considered a single day). Highlighted panels and blue circles represent observations. Solid lines curves represent the average over the MaxEnt reweighted ensemble of trajectories (8192 samples), and the shaded areas represent the $\pm 33\%$ and $\pm 67\%$ quantiles. Model predictions match well with *ground-truth* trajectories ($D_{\text{KL}}^{\text{traj}} = 8 \times 10^{-3}$).

varying the infection seed across different spatial patches, as well as accounting for a small variance in the mobility flows. Finally, MaxEnt reweights the ensemble trajectories, maximizing entropy subject to the observations, and determines the most probable state of the network. We consider a Laplace distribution prior [Eq. (2)] with standard deviation of 1 to allow some disagreement between the MaxEnt fit and the observations. The MaxEnt implementation is done using Adam optimizer [92] with initial learning rate of 10^{-2} and reduced learning rate on plateau callback (factor of 0.9, patience of 10 and minimum learning rate of 10^{-4}) for 1000 epochs. To assess the model's performance, we compare the predictions against a simulated *ground-truth* trajectory derived from known preselected epidemiological parameters. Knowledge of the *ground truth* enables a proof-of-concept analysis to assess model performance under different scenarios. The ones we consider are density of the network, temporal window of observations, the number of observations, use of less complex compartmental schemes for inference, and variations in mobility flow of observations with respect to the infection seeded origin. As performance metrics we consider the following:

(i) Forward dynamics: To compare the predicted trajectory against the known *ground-truth* trajectory we measure the KL divergence, defined as

$$D_{\text{KL}}^{\text{traj}} = -\frac{1}{TN_p} \sum_{t=0}^T \sum_{i=1}^{N_p} \sum_m \rho_i^m(t) \log \left[\frac{\rho_i^m(t)}{\hat{\rho}_i^m(t)} \right]. \quad (17)$$

Here T is the total time in the epidemic trajectory and m is the label for the compartments. The term $\hat{\rho}_i^m(t)$ is the model's prediction for the probability of an individual associated with

the patch i to belong to a compartment m at time t and $\rho_i^m(t)$ is the corresponding value for the *ground-truth* trajectory.

(ii) Backward dynamics: The accuracy of the model in making the correct prediction with respect to the ground-truth source of infection (P_0). This can be treated as a binary multiclass classification problem, where the correct prediction of the true origin node is regarded as the *true positive* (TP) class and every other prediction falls into the *false positive* (FP) class. Given this, the accuracy (α) is defined as

$$\alpha = \frac{TP}{TP + FP}. \quad (18)$$

The posterior probabilities P_0 for nodes are obtained by summing over the MaxEnt posterior weights for each node seeded as the infection source—compartment E—in the sampled trajectories ensemble at $t = 0$, and the largest value among the set corresponds to P_0 probability. To assess performance, we use the top- k posterior probabilities P_0 , and the frequency of *true positive* predictions as our metric. For instance, for $k = 5$, the model's prediction for P_0 is classified as a *true positive* if the infection source is among the top five values of P_0 probabilities and a *false positive* otherwise.

We employ our method on two systems: a synthetic metapopulation network and the mobility network of New York State at the resolution of counties.

A. Synthetic contact networks

The 10-node metapopulation ($N_p = 10$) is represented as a directed graph in Fig. 3(a), where each node (patch) in the network represents a town or city in the metapopulation and the directed edges account for mobility flows between them.

TABLE I. Distributions of input parameters for the synthetic contact network *ground-truth* trajectory.

Parameter	Distribution	Mean	Std	Min	Max
Area (a_i)	Normal	2×10^3	10^3	300	—
Populations (n_i)	Normal	5×10^5	3×10^5	0	—
T_{ij} ($i = j$)	Normal	10^5	3×10^3	0	—
T_{ij} ($i \neq j$)	Normal	10^2	5×10^1	0	—

The nodes are connected at random with a connection probability $\tau = 0.4$, such that on average each node is connected to four other patches (considering both in- and out-flows). The area of each node, the population, and entries of the mobility matrix are sampled from normal distributions with parameters listed in Table I.

The infection is initially seeded in patch 1 [node with the yellow edge in Fig. 3(a)] with a single individual exposed to the disease at $t = 0$. The parameters for this *ground-truth* trajectory are chosen to be $\beta' = 0.025$, $\beta = 0.05$, $\epsilon = 0.6$, $\eta = \frac{1}{1.2}$, and $\mu = \frac{1}{7}$. In Fig. 3(b) we show as dashed curves the trajectory of the *ground-truth* SEAIR model for all 10 nodes for a period of $T = 250$ days. We define a distribution of the parameters and explore the trajectory space. These distributions and their Kernel density estimation plots can be found in Table S1 and Fig. S1 in the Supplemental Material [93]. For all 8192 sampled trajectories, we assume a uniform probability of infection, and randomly choose a patch, and an individual in that patch as the infection seed (see Fig. S2 in the Supplemental Material [93]). For observations, we consider a total of 50 data points (weekly averages) from the I and R compartments within an observation window of (50 140) days. The highlighted panels and blue circles in Fig. 3(b) mark the five randomly chosen patches and the observations, respectively.

We use the MaxEnt framework, to reweight the ensemble of trajectories to agree best with the observed data points and obtain the P_0 probability by summing all the weights for each exposed node in the sampled trajectories at $t = 0$. The reweighted average over the sampled trajectories are shown as solid curves in Fig. 3(b), and the shaded area marks the $\pm 33\%$ and $\pm 67\%$ quantiles. The calculated $D_{\text{KL}}^{\text{traj}}$ of 8×10^{-3} indicates close agreement between model predictions and the *ground-truth* trajectory. In Fig. 3(a) we also show nodes colored by their value of P_0 probability, indicating that the algorithm predicts node 1 (the true origin of infection) as the most probable source with a certainty of 76%.

1. Effect of network density

Next, we check the accuracy of the model as a function of the density of connections between nodes. We tune the connection probability in the range $0.25 \leq \tau \leq 1$ to sample the spectrum between a sparse and fully connected network. We redo our simulations over 8000 different networks in this range and for each trajectory choose a random node from which to seed the infection. All other relevant parameters are kept the same. In Fig. 4(a) we plot $D_{\text{KL}}^{\text{traj}}$ as a function of τ , where the solid lines indicate the mode over 200 samples for a given τ , and the shaded areas mark the 30% confidence interval. The region marked in green corresponds to

the true positive (*TP*) where the algorithm correctly identifies the true infection seed as the most probable source, whereas the region marked in blue corresponds to false positive (*FP*) when the true source was not identified as the most probable. Here we use a $k = 1$ acceptance criteria, a rather stringent condition, as even when the true source is identified as the second most probable, it is still marked *FP*. The low values of $D_{\text{KL}}^{\text{traj}}$ indicates that irrespective of the correct identification of the infection seed, the predicted and *ground-truth* trajectories match well, independent of network density. Note that this is true for the chosen observations obtained in the (50,140) day temporal window and will be further discussed later.

Additionally, we find high values of P_0 for *TP* that are (mostly) independent of the graph connection probability τ , while for *FP*, we find low values of P_0 that get progressively worse with increasing τ [Fig. 4(b)]. This means that our model is far more confident in its *TP* predictions compared to the *FP* ones. The model's calibration is assessed in the reliability diagram shown in Fig. 4(c), where we plot the accuracy α as a function of P_0 . The case of a perfectly calibrated model, where α changes linearly with certainty, is shown as the orange dashed line. The figure indicates that the model is more accurate than it believes in a conservative manner. Finally, in Fig. 4(d) we plot α as a function of τ finding that the model's performance degrades in high-density networks, which is to be expected given that dense networks have more complexity in their mobility flows. Nevertheless, at worst, the model shows $\approx 60\%$ accuracy in a fully connected graph. Indeed, for a wide range of connection probabilities (corresponding to realistic settings) we find an accuracy in the range of 80–90%.

2. Effect of temporal window of observations

Next we evaluate the model's performance as a function of the temporal window in which observations are made. Current understanding of epidemic dynamics suggests that contact-tracing is effective only in the initial stages of the outbreak, and any information on the infection source is lost at later times. Indeed, in Ref. [51] an approximation to this temporal horizon, t_{hor} , was derived for the SIR model. Adapting the formulation to the SEAIR model leads to an expression of the form:

$$t_{\text{hor}} = \lambda_{\text{max}}^{-1} \log \left(\frac{N^{\text{TOT}}}{c_{\text{max}}} \right), \quad (19)$$

where λ_{max} corresponds to the leading eigenvalue of the linearized system of ODEs governing the evolution of the dynamics and c_{max} a constant needed to fix the infectious seeds at the beginning of the outbreak (see Appendix A for a complete derivation). We consider a sparse ($\tau = 0.4$) and dense ($\tau = 1.0$) network and check for the presence of such a

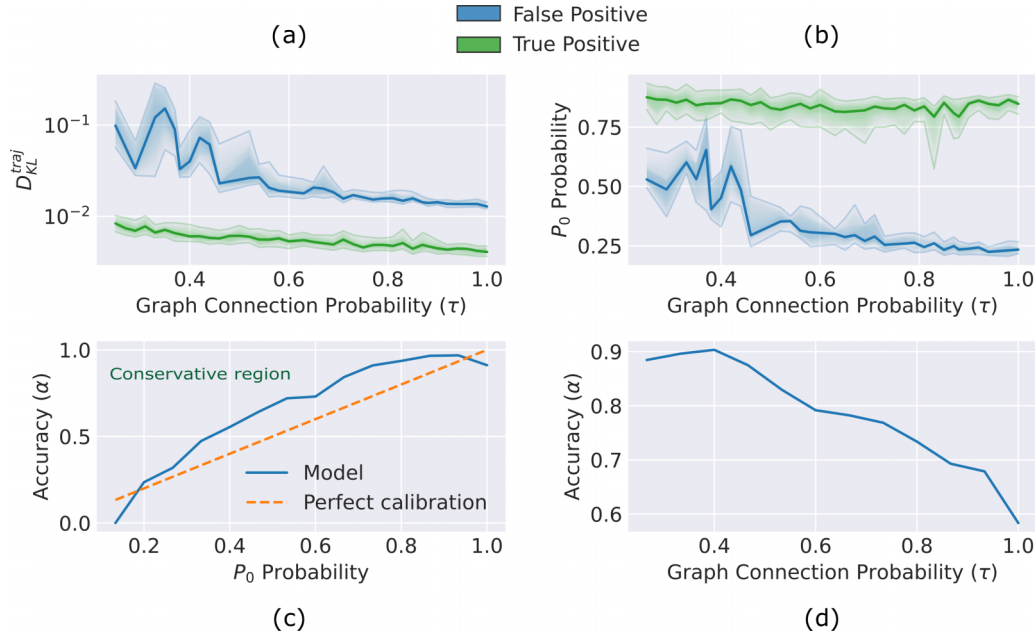


FIG. 4. Effect of network density on model performance. Epidemic evolution on 8000 synthetic metapopulation networks with connection probabilities in the range $0.25 \leq \tau \leq 1.0$. All other parameters kept the same. (a) Performance of forward dynamics, D_{KL}^{traj} as a function of τ . Solid lines indicate the mode, and the shaded areas mark shows the 30% confidence interval. Green marks where the model indicates the true seed as the most probable infection source and blue otherwise. (b) The P_0 probability as a function of τ , lines and shaded regions are the same as in (a). (c) Reliability diagram for the model, where the dashed line represents a perfectly calibrated model where accuracy α changes linearly with certainty. The model’s predictions fall into the conservative region (above the orange dashed line), suggesting that it is more accurate than it believes. The expected calibration error (mean absolute calibration error) between our model and a perfectly calibrated model is 0.123. (d) Accuracy α as a function of the connection probability τ , indicating a performance drop as one moves from sparse to dense graphs (given the same number of observations).

temporal horizon by shifting the 5-week observation period within the range $T = 250$, collecting 50 data points (5 points from each of compartments I and R for 5 random nodes). As a robustness check, we exclude the true-infection source from our observed samples. In Figs. 5(a) and 5(b), we plot D_{KL}^{traj} and P_0 as a function of the midpoint of observations for each

5-week window (200 sample runs in each bin), where curves indicate the mode and shapes refer to dense (circles) and sparse (inverted triangles) networks. Curves are split into TP (green) and FP (blue). In the figure, we show the $k = 3$ acceptance criteria, and in Fig. S3 in the Supplemental Material [93] we show the case for a $k = 1$ acceptance criteria. In Fig. 5(c),

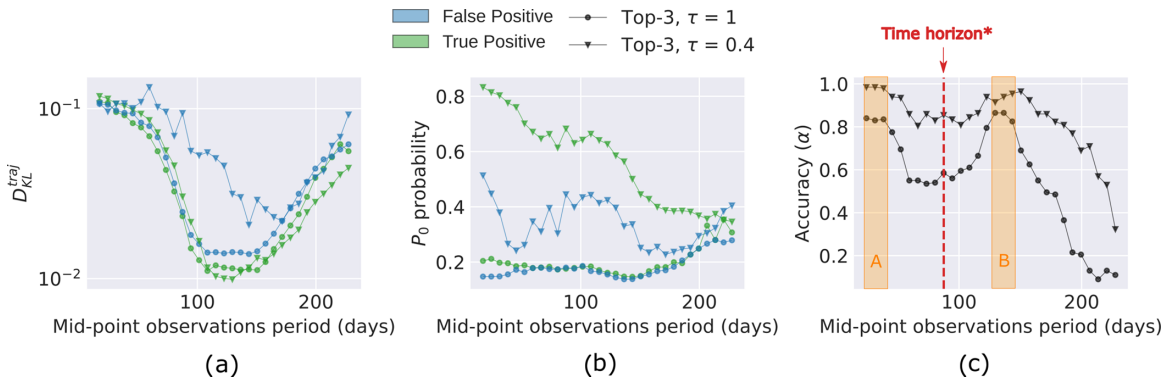


FIG. 5. Effect of observations temporal window on model performance. Epidemic evolution on 8000 synthetic metapopulation sparse and dense networks, with τ of 0.4 and 1.0, respectively. Green shows true positive predictions and blue accounts for false positives in sparse (triangle) and dense (circle) networks, given a top-3 acceptance criteria. Each point in panels (a) and (b) represent the mode over 200 samples at the corresponding midpoint observation period. (a) Forward dynamics predictions assessment using D_{KL}^{traj} between the MaxEnt reweighted trajectory and *ground truth*. (b) Mode values for the P_0 probabilities. (c) Accuracy vs midpoint observation period. The model’s accuracy drops as observations are obtained from time values beyond early stages of the outbreak (stage A) but increases again at more advanced time periods (stage B) and beyond the time horizon (t_{hor}), where t_{hor} (adapted from Ref. [51]) is a reported fundamental limit beyond which no algorithm can detect the true origin of infection.

we plot the accuracy α as a function of the midpoint of observations. As expected, the figure indicates high accuracy at the early stages of the outbreak (marked Region A), and decreases as the epidemic progresses. Considering the set of parameters $(\beta, \beta', \mu, \langle k \rangle, \epsilon, \eta) = (0.05, 0.025, \frac{1}{7}, 10, 0.6, \frac{1}{1.2})$ and a seed composed of a single exposed individual at the beginning of the outbreak, we obtain $c_{\max} = 0.372$ and $t_{\text{hor}} = 90.9$ days marked as a red vertical dashed line.

Surprisingly, as one crosses t_{hor} a nonmonotonic trend is observed and a new peak in the accuracy is observed at later times ($t \approx 150$) in both sparse and dense networks, marked as Region B. To the best of our knowledge, this peak in accuracy at advanced stages of the epidemic evolution, where information can be recovered on the infection source, has not been reported before. Indeed, this region also corresponds to the lowest values of $D_{\text{KL}}^{\text{traj}}$ indicating the closest match to the *ground-truth* trajectory and thus an optimal window in which to simultaneously infer the most accurate information in forward and backward dynamics [in Figs. 5(a) and 5(b), respectively]. A possible explanation for this phenomenon is that it corresponds to the regions with the highest gradients in epidemic curves [Fig. 3(b)], whereas the low gradients of the trajectories at other values of t provides the model with insufficient information to perform a reliable inference. Moreover, given that the number of contacts across the metapopulation is pretty homogeneous, as dictated by Eq. (12), one can expect a roughly homogeneous duration of the SIR outbreaks in all the patches. This homogeneity entails that the order at which outbreaks die out across the metapopulation respects the arrival of the pathogen at the early stage of the dynamics.

3. Epidemiological model-agnostic inference

Next, we try benchmarking the prediction performance of our approach, with a simpler inference compartmental model, compared to the compartmental scheme used to generate the *ground-truth* trajectory. In this setting, the *ground truth* is generated based on SEAIR, whereas the inference model for sampling trajectories uses a simple SIR scheme. The main differences between both compartmental models is that in the SIR model scheme, susceptible agents become symptomatic and infectious on contagion from other infectious counterparts, therefore neglecting both the latent period and the existence of asymptomatic individuals. We run an exhaustive analysis by adjusting connection probability (τ) and acceptance criteria for the true positive identification. We consider a sparse ($\tau = 0.4$) and dense ($\tau = 1.0$) network and use a top-1 and top-3 evaluation setting. Prediction accuracies for this analysis are shown in Table II.

The accuracies reported in each row are based on 8000 simulations, where the infection is seeded randomly in a 10-node synthetic mobility network with five nodes observed in temporal window and parameters similar to the ones used in Sec. III A 1. Using a simple SIR compartmental scheme, the stringent top-1 accuracy scores are consistent with was reported earlier in Fig. 4(d). This suggests that the MaxEnt approach can still provide a reliable inference on the spatial source of the seeded infection, regardless of lacking complete knowledge on more complicated epidemiological models that better capture the disease dynamics. Note that the runs with

TABLE II. Model-agnostic performance with simpler inference compartmental models. Benchmarking prediction performance with simple SIR inference compartment models with respect to an SEAIR *ground-truth* model. Each row represents results from 8000 simulations, where node connection probability (τ) and true positive acceptance criteria are adjusted.

τ	Acceptance	Inference model	Accuracy
1.0	Top-1	SIR	0.564
1.0	Top-3	SIR	0.784
0.4	Top-1	SIR	0.970
0.4	Top-3	SIR	0.993

the less strict top-3 acceptance criteria have higher accuracy scores. This trend is expected and suggests that higher accuracy scores are achievable by increasing the number of observations (see Sec. III B 1).

B. Mobility network of New York State

In this section, we apply our formalism to characterize the spread of infectious diseases across a real metapopulation, the network of commuters across New York State at the spatial resolution of counties, of which there are 62. The mobility flows between counties, as well as their respective areas and populations, are obtained from the United States LODS commuting database [94]. Our focus here is on assessing the performance of the method in detecting the spatial location of the infection seed given more complex and realistic mobility patterns. We first generate the *ground-truth* trajectory according to the following epidemic parameters: $\beta' = 0.029$, $\beta = 0.052$, $\epsilon = 0.586$, $\eta = \frac{1}{2.493}$, $\langle k \rangle = 10$, and $\mu = \frac{1}{1.49}$ and then collect observations corresponding to weekly averages of populations in compartments I and R. Observations are collected from specific counties and are drawn from the (60,140) day temporal window. Once again, we define a distribution of the parameters according to Table S1 [93] and explore the trajectory space by generating an ensemble of 65 536 different realizations as the MaxEnt prior.

1. Effect of the number of observations

Given that the number of observations is directly linked to epidemic surveillance efforts, we first check the performance of our model as a function of the number of counties from which data are collected. Specifically, we test the accuracy of identifying the correct spatial origin of the infection seed as we increase the number of counties observed. We choose three counties with different population densities in which to seed the infection: Hamilton (2.74 per square mile), Monroe (1.14×10^3 per square mile), and Kings (3.72×10^4 per square mile). We collect 10 samples from each county (randomly chosen) and vary the number of counties observed from 1, 5, and 25. We do not necessarily exclude the seed counties from our randomly chosen observations.

In Fig. 6 we plot the counties colored according to their values of the posterior probability P_0 . The top row represents observations from a single county, the middle row from 5 counties and the bottom row 25 counties. The true origin is marked as a downward yellow triangle and the observations

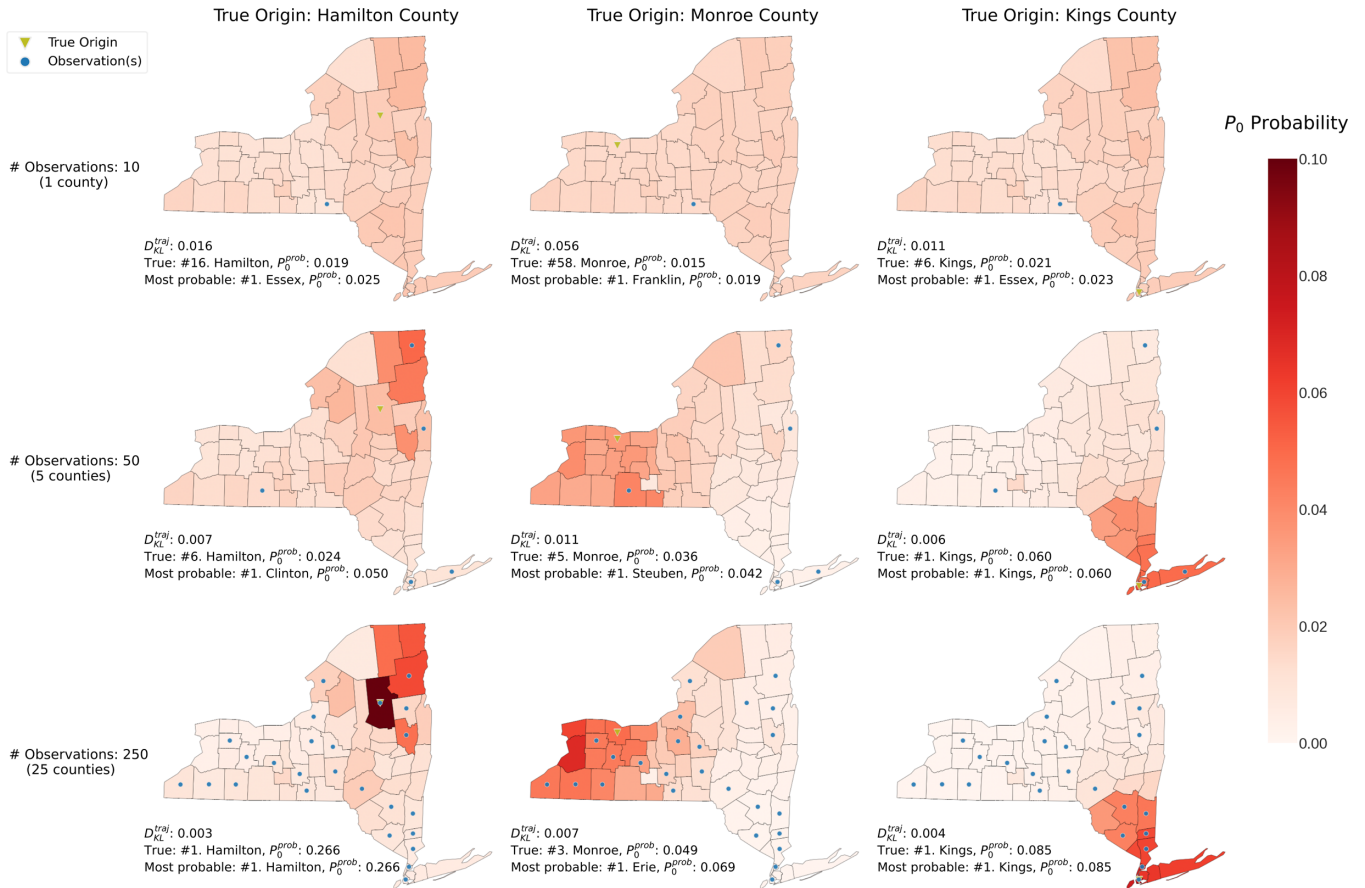


FIG. 6. Effect of number of observations on model performance. Epidemic evolution in the real mobility network of New York State. The yellow downward triangle represents the true origin of infection, and blue circles show the counties observed. The P_0 predictions are ranked based on their probabilities. The most probable and true origin ranks, as well as the D_{KL}^{traj} values, are shown for each simulation. For example, in the simulation with Kings County as the true origin with 10 observations, model's most probable prediction for the infection source is Essex County with P_0^{prob} of 0.023, while the true origin is ranked sixth with P_0^{prob} of 0.021. Starting from the first row to bottom, with the increase of the number of observations, the model is able to infer the true origin of P_0 among the top-5 most probable predictions and obtain a well fit to the *ground-truth* trajectory, balancing both future and backward dynamics predictions.

by blue circles. The three columns correspond to the different infection seeds. In each case, we show D_{KL}^{traj} , P_0 for the true origin and how the model ranks it as a likely source of infection, as well as the model's prediction for the top-ranked county in terms of the posterior probability P_0 . For all three infection sources, observations from a single county yields poor results for D_{KL}^{traj} , and the model ranks the true origin quite low as a probable source (16 for Hamilton, 58 for Monroe, and 6 for Kings). Sampling from 5 counties results in a considerable increase in performance for the first two counties (6 for Hamilton and 5 for Monroe), while for Kings the model correctly identifies it as the most likely origin. We also note about an order of magnitude decrease in D_{KL}^{traj} for all three counties, indicating good agreement with the forward dynamics. Finally, sampling from 25 counties results in the best performance, where in addition to Kings, the model correctly identifies Hamilton as a true infection source, while for the case of Monroe the model ranks it as the third most likely origin. We see further improvements in matching the forward dynamics with further decreases in D_{KL}^{traj} (about two orders of magnitude as compared to observing as single county). As

an illustrative example, we show the full trajectory set for Monroe County true origin with 250 observations in Fig. S4 in the Supplemental Material [93].

We note the difference in accuracy of the model when assessing Hamilton and Monroe counties. Hamilton, despite being a much more sparsely populated area than Monroe, was correctly identified as the true source, whereas Monroe was ranked third. The reason for this discrepancy is that Hamilton was also included in the sample of 25 counties as an input to the model, whereas Monroe was excluded from its observation set. The likelihood of the model to correctly guess the true source increases greatly when the source itself is included as an observation, a feature also seen in our synthetic metapopulation networks. On the other hand, the ability of the model to identify Monroe as the third most likely source is notable, given that no information on Monroe was available to the model. Indeed, Erie County, adjacent to Monroe, was marked as the most likely source of infection. Kings County is an outlier compared to the other two, in a sense that already with a single observed county, the model marked it amongst the upper 10% of posterior probabilities P_0 . Certainly there are more people in Kings (it has the highest population density

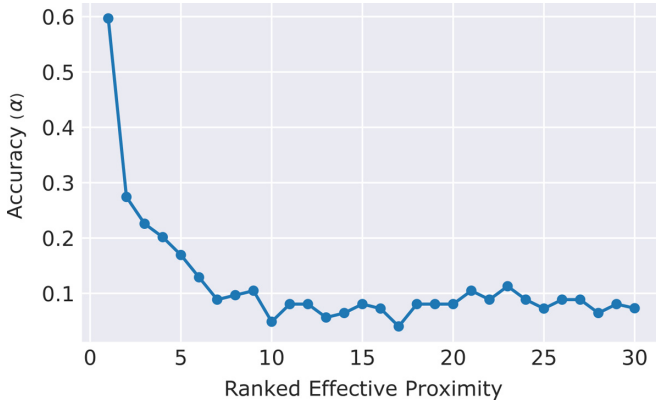


FIG. 7. Effect of mobility-strength between counties on accuracy in the mobility network of New York State. The accuracy of the model as a function of the *effective proximity* ϕ [Eq. (20)]. Each point represents the average over 180 runs of the model with a randomly selected true origin county and 10 sampled trajectories from a single county. The horizontal axis corresponds to the ranking of the values of ϕ . Rank-1 corresponds to the case when the observations are made from the source county.

by far among the three counties), but also it is coterminous with Brooklyn, and a popular destination for residents of other counties. Therefore, there is a higher likelihood of mixing of populations from different parts of the state.

2. Dependence of accuracy on effective proximity

Given the latter observation, we next check whether the strength of mobility flows (both in and out) between counties plays a role in the model's accuracy. Two locations are strongly connected if there are many people traveling between them, and therefore we define an *effective proximity* matrix ϕ with elements given by

$$\phi_{ij} = \frac{1}{R_{ij} + R_{ji}}, \quad (20)$$

where R is the mobility matrix, and we take into account both in- and out-flows. In this setting, counties that are strongly connected by mobility flows have low values of ϕ_{ij} and are therefore more proximal in mobility space. We next seed the infection in location i and sample from a single county j (including the source), ranked in increasing order according to their value of ϕ_{ij} with the rank of i corresponding to 1. We then generate 8000 trajectories with a randomly sampled true origin and plot the accuracy α as a function of effective proximity to the origin county in Fig. 7. Each point in the figure corresponds to the average over 180 realizations. We clearly see a monotonically decreasing trend; sampling from counties further away from the origin-county leads to a sharp decline in accuracy, saturating at around the seventh furthest county. The trend is expected, given that locations further away from the source in mobility space, experience delays in arrivals of infectious cases. This lag results in the observation of degenerate epidemic trajectories, thus making the inference less accurate.

IV. CONCLUSIONS

This paper has provided a systematic study of both backward and forward dynamics inference on contagion process in contact networks. We have applied the statistical mechanics principle of maximum entropy to the conventional SEAIR epidemiology models to reweight disease trajectories and obtain the best fit to a set of observations, while making reliable predictions on the true source of the outbreak. The novelty of this work lies within working well under the sparse-data regime and highly uncertain initial parameter priors, making our method highly suitable for studying disease dynamics. Finally, the method proposed here is independent of the underlying compartmental model. While we presented our work in the context of epidemics, the approach is easily generalizable to similar classes of spreading processes. For example, a single computer virus can infect millions of other computers through the Internet. An isolated failure in an electrical power grid network can result a citywide blackout. Misinformation or a baleful rumor can spread through social networks and cause terror and inconvenience. In all these scenarios, the contagion process [95,96] could identify the source of the risk on the network and quarantine its harmful effects [97–100].

The MaxEnt implementation is publicly available on Github [101] as a Python package called maxent and it can be applied to any simulator. The SEAIR model used in this work is publicly available as Python package called py0 on Github [102].

ACKNOWLEDGMENTS

We thank the Center for Integrated Research Computing (CIRC) at University of Rochester for providing computational resources and technical support. Funding for this research was provided by National Science Foundation under Grant No. 2029095. D.S.-P. acknowledges financial support from Spanish Ministerio de Ciencia e Innovación (Projects No. FIS2017-87519-P and No. PID2020-113582GB-I00), from the Departamento de Industria e Innovación del Gobierno de Aragón y Fondo Social Europeo (FENOL group E-19), and from Fundación Ibercaja and Universidad de Zaragoza (Grant No. 224220).

APPENDIX: DERIVATION FOR TIME HORIZON

One of the key findings in this work is the nonmonotonic trend found for the time dependence of the accuracy of patient-zero identification. This result is in sharp contrast with other findings published in Refs. [51,103], suggesting that such accuracy should monotonically decrease with time because of the degeneracy of the epidemic trajectories. Specifically, in the latter manuscript, the authors derive an estimation for the so-called time horizon, beyond which patient-zero identification becomes infeasible. For the sake of comparison, we now adapt the derivation of the t_{hor} value to our compartmental model, according to the same rationale followed in Ref. [51]. Mathematically, the authors define the time horizon as the time at which the number of infectious individuals scales to the entire population. To derive

it, the authors neglect the nonlinear terms governing the evolution of the number of infected individuals. This assumption simplifies the mathematical analysis at the expense of underestimating the duration of the outbreak and, consequently, the estimation of the time horizon. This occurs because the nonlinear terms involved in the contagions of SIR-like dynamics slow down the late advance of the outbreak.

Being aware of the limitations posed by the assumptions made to derive the time horizon, for the sake of comparison, we now proceed to adapt the derivation made by the authors in Ref. [51] to our compartmental dynamics. First, it is useful to consider a mean-field scenario and neglect the contact heterogeneities existing across the different patches of the metapopulation. At this limit, the dynamics is completely characterized by the fraction of the population in each compartment m at each time step t , denoted in the following by $\rho^m(t)$. Specifically:

$$\rho^S(t+1) = [1 - \Pi(t)]\rho^S(t), \quad (\text{A1})$$

$$\rho^E(t+1) = (1 - \eta)\rho^E(t) + \rho^S(t)\Pi(t), \quad (\text{A2})$$

$$\rho^A(t+1) = (1 - \epsilon)\eta\rho^E(t) + (1 - \mu)\rho^A(t), \quad (\text{A3})$$

$$\rho^I(t+1) = \epsilon\eta\rho^E(t) + (1 - \mu)\rho^I(t), \quad (\text{A4})$$

$$\rho^R(t+1) = \rho^R(t) + \mu[\rho^I(t) + \rho^A(t)], \quad (\text{A5})$$

with

$$\Pi(t) = 1 - (1 - \beta)^{\langle k \rangle \rho^I(t)} (1 - \beta')^{\langle k \rangle \rho^A(t)}, \quad (\text{A6})$$

At the early stages of the outbreak, the number of affected individuals is negligible compared with the size of the population. Therefore, we can assume that $\rho^m \ll 1$, with $m = \{E, A, I, R\}$. This turns the latter expression into:

$$\Pi(t) \simeq \langle k \rangle [\beta \rho^I(t) + \beta' \rho^A(t)], \quad (\text{A7})$$

where we have considered that $\beta, \beta' \ll 1$ as well. Introducing the latter expression into Eq. (A2) and neglecting $\mathcal{O}(\rho^2)$ terms

lead to

$$\rho^E(t+1) = (1 - \eta)\rho^E(t) + \beta \langle k \rangle \rho^I(t) + \beta' \langle k \rangle \rho^A(t). \quad (\text{A8})$$

For the sake of simplicity, it is convenient at this point to rewrite the equations in terms of the occupation of each compartment m , denoted by $m(t)$. In particular, restricting ourselves to the infectious or potentially infectious individuals, we have that

$$\dot{E} = -\eta E + \beta' \langle k \rangle A + \beta \langle k \rangle I, \quad (\text{A9})$$

$$\dot{A} = (1 - \epsilon)\eta E - \mu A, \quad (\text{A10})$$

$$\dot{I} = \epsilon\eta E - \mu I, \quad (\text{A11})$$

where we have defined $\dot{m} = m(t+1) - m(t)$. Consequently, the evolution of the system is given by:

$$\vec{m}(t) = \sum_{i=1}^3 c_i \vec{v}_i e^{\lambda_i t}, \quad (\text{A12})$$

being λ_i and \vec{v}_i each of the eigenvalues and their associated eigenvectors respectively and c_i the integration constants needed to fix the initial conditions to run the dynamics. Albeit the latter expression constitutes the exact evolution of the system, the long-term dynamics is completely determined by the largest eigenvalue λ_{\max} and its associated eigenvector \vec{v}_{\max} . Therefore, we can assume that:

$$\vec{m}(t) \approx c_{\max} \vec{v}_{\max} e^{\lambda_{\max} t}, \quad (\text{A13})$$

with

$$\lambda_{\max} = \frac{\sqrt{(\eta - \mu)^2 + 4\langle k \rangle \eta [(1 - \epsilon)\beta' + \epsilon\beta]} - (\eta + \mu)}{2}. \quad (\text{A14})$$

Without loss of generality, we set the component of the eigenvector associated with the symptomatic infectious compartment to $v'_{\max} = 1$. Finally, equating the number of symptomatic infectious individuals to the population size, we derive the time horizon t_{hor} which reads as:

$$t_{\text{hor}} = \lambda_{\max}^{-1} \log \left(\frac{N^{\text{TOT}}}{c_{\max}} \right). \quad (\text{A15})$$

-
- [1] E. Estrada, *Phys. Rep.* **869**, 1 (2020).
[2] World Health Organization, Coronavirus Disease 2019 (COVID-19): Situation Report, 72, Technical Report (2020), <https://apps.who.int/iris/handle/10665/331685>.
[3] S. Hazarie, D. Soriano-Paños, A. Arenas, J. Gómez-Gardeñes, and G. Ghoshal, *Commun. Phys.* **4**, 191 (2021).
[4] D. D. S. Candido, A. Watts, L. Abade, M. U. Kraemer, O. G. Pybus, J. Croda, W. De Oliveira, K. Khan, E. C. Sabino, and N. R. Faria, *J. Travel Med.* **27**, taaa042 (2020).
[5] M. Chinazzi, J. T. Davis, M. Ajelli, C. Gioannini, M. Litvinova, S. Merler, A. P. y Piontti, K. Mu, L. Rossi, K. Sun *et al.*, *Science* **368**, 395 (2020).
[6] M. Gilbert, G. Pullano, F. Pinotti, E. Valdano, C. Poletto, P.-Y. Boëlle, E. d'Ortenzio, Y. Yazdanpanah, S. P. Eholie, M. Altmann *et al.*, *Lancet* **395**, 871 (2020).
[7] V. Abedi, O. Olulana, V. Avula, D. Chaudhary, A. Khan, S. Shahjouei, J. Li, and R. Zand, *J. Racial Ethnic Health Dispar.* **8**, 732 (2021).
[8] F. Ahmed, N. Ahmed, C. Pissarides, and J. Stiglitz, *Lancet Publ. Health* **5**, e240 (2020).
[9] H. Barbosa, S. Hazarie, B. Dickinson, A. Bassolas, A. Frank, H. Kautz, A. Sadilek, J. Ramasco, and G. Ghoshal, *Sci. Rep.* **11**, 8616 (2021).
[10] B. J. Berry, in *Urban Ecology* (Springer, Berlin, 2008), pp. 25–48.
[11] L. Bertinelli and D. Black, *J. Urb. Econ.* **56**, 80 (2004).
[12] M. U. Kraemer, C.-H. Yang, B. Gutierrez, C.-H. Wu, B. Klein, D. M. Pigott, L. Du Plessis, N. R. Faria, R. Li, W. P. Hanage *et al.*, *Science* **368**, 493 (2020).
[13] B. F. Maier and D. Brockmann, *Science* **368**, 742 (2020).

- [14] M. Gatto, E. Bertuzzo, L. Mari, S. Miccoli, L. Carraro, R. Casagrandi, and A. Rinaldo, *Proc. Natl. Acad. Sci. USA* **117**, 10484 (2020).
- [15] A. Aleta, D. Martín-Corral, A. Pastore y Piontti, M. Ajelli, M. Litvinova, M. Chinazzi, N. E. Dean, M. E. Halloran, I. M. Longini, S. Merler, A. Pentland, A. Vespignani, E. Moro, and Y. Moreno, *Nat. Hum. Behav.* **4**, 964 (2020).
- [16] J. Dehning, J. Zierenberg, F. P. Spitzner, M. Wibral, J. P. Neto, M. Wilczek, and V. Priesemann, *Science* **369**, eabb9789 (2020).
- [17] R. M. Anderson and R. M. May, *Infectious Diseases of Humans: Dynamics and Control* (Oxford University Press, Oxford, 1992).
- [18] M. J. Keeling and P. Rohani, *Modeling Infectious Diseases in Humans and Animals* (Princeton University Press, Princeton, NJ, 2011).
- [19] E. Vynnycky and R. White, *An Introduction to Infectious Disease Modelling* (Oxford University Press, Oxford, 2010).
- [20] M. T. Meehan, D. P. Rojas, A. I. Adekunle, O. A. Adegboye, J. M. Caldwell, E. Turek, B. Williams, J. M. Trauer, and E. S. McBryde, *Paediatric respiratory reviews* (2020).
- [21] K. Roosa and G. Chowell, *Theor. Biol. Med. Modell.* **16**, 1 (2019).
- [22] M. Castro, S. Ares, J. A. Cuesta, and S. Manrubia, *Proc. Natl. Acad. Sci. USA* **117**, 26190 (2020).
- [23] C. O. Wilke and C. T. Bergstrom, *Proc. Natl. Acad. Sci. USA* **117**, 28549 (2020).
- [24] N. P. Jewell, J. A. Lewnard, and B. L. Jewell, *J. Am. Med. Assoc.* **323**, 1893 (2020).
- [25] A. Pandey, A. Mubayi, and J. Medlock, *Math. Biosci.* **246**, 252 (2013).
- [26] M. Lavielle, A. Samson, A. Karina Fermin, and F. Mentré, *Biometrics* **67**, 250 (2011).
- [27] L. F. New, J. Matthiopoulos, S. Redpath, and S. T. Buckland, *Am. Nat.* **174**, 399 (2009).
- [28] A. Morton and B. F. Finkenstadt, *J. Roy. Stat. Soc.: C (Appl. Stat.)* **54**, 575 (2005).
- [29] S. Cauchemez and N. M. Ferguson, *J. R. Soc. Interface* **5**, 885 (2008).
- [30] A. S. Talawar and U. R. Aundhakar, *Glob J. Pure. Appl. Math.* **12**, 1299 (2016).
- [31] D. He, E. L. Ionides, and A. A. King, *J. R. Soc. Interface* **7**, 271 (2010).
- [32] A. A. King, E. L. Ionides, M. Pascual, and M. J. Bouma, *Nature (Lond.)* **454**, 877 (2008).
- [33] E. L. Ionides, C. Bretó, and A. A. King, *Proc. Natl. Acad. Sci. USA* **103**, 18438 (2006).
- [34] H. Bock, Recent advances in parameter identification techniques for ode Heidelberg, Federal Republic of Germany (1983).
- [35] N. Arora and L. T. Biegler, *Comput. Optim. Appl.* **28**, 51 (2004).
- [36] H. T. Banks, J. A. Burns, and E. M. Cliff, *SIAM J. Contr. Optimiz.* **19**, 791 (1981).
- [37] M. S. Ciupe, B. L. Bivort, D. M. Bortz, and P. W. Nelson, *Math. Biosci.* **200**, 1 (2006).
- [38] L. T. Biegler, J. J. Damiano, and G. E. Blau, *AIChE J.* **32**, 29 (1986).
- [39] R. Yang, R. Liu, K. Xu, Y. Yang, G. Dong, and W. Zhang, *Anal. Methods* **5**, 5949 (2013).
- [40] G. Hooker, S. P. Ellner, L. D. V. Roditi, and D. J. D. Earn, *J. R. Soc. Interface* **8**, 961 (2011).
- [41] M. G. B. Blum and C. Tran, *Biostatistics* **11**, 644 (2010).
- [42] T. Toni, D. Welch, N. Strelkowa, A. Ipsen, and M. P. Stumpf, *J. R. Soc. Interface* **6**, 187 (2009).
- [43] T. Kypraios, P. Neal, and D. Prangle, *Math. Biosci.* **287**, 42 (2017).
- [44] T. Rogalsky, Bézier control parameterization for evolutionary optimization in disease models, in *Proceedings of the 14th Annual Conference Companion on Genetic and Evolutionary Computation*, GECCO '12 (Association for Computing Machinery, USA, 2012), pp. 523–530. (2012).
- [45] D. Iacoviello and G. Liuzzi, *Int. J. Simul. Model.* **7**, 81 (2008).
- [46] G. Streftaris and G. J. Gibson, *Stat. Model.* **4**, 63 (2004).
- [47] D. Clancy and P. D. O'Neill, *Bayes. Anal.* **3**, 737 (2008).
- [48] N. Demiris and P. D. O'NEILL, *Scand. J. Stat.* **32**, 265 (2005).
- [49] F. Altarelli, A. Braunstein, L. Dall'Asta, A. Lage-Castellanos, and R. Zecchina, *Phys. Rev. Lett.* **112**, 118701 (2014).
- [50] H. El Maroufy, T. Kernane, S. Becheket, and A. Ouddadj, *J. Stat. Comput. Simul.* **86**, 2229 (2016).
- [51] C. Shah, N. Dehmamy, N. Perra, M. Chinazzi, A.-L. Barabási, A. Vespignani, and R. Yu, *arXiv:2006.11913* (2020).
- [52] Z. Shen, S. Cao, W.-X. Wang, Z. Di, and H. E. Stanley, *Phys. Rev. E* **93**, 032301 (2016).
- [53] P. C. Pinto, P. Thiran, and M. Vetterli, *Phys. Rev. Lett.* **109**, 068702 (2012).
- [54] F. Marinelli and J. D. Faraldo-Gómez, *Biophys. J.* **108**, 2779 (2015).
- [55] A. Cesari, S. Reißer, and G. Bussi, *Computation* **6**, 15 (2018).
- [56] D. B. Amirkulova and A. D. White, *Mol. Simul.* **45**, 1285 (2019).
- [57] B. Shipley, D. Vile, and É. Garnier, *Science* **314**, 812 (2006).
- [58] J. Harte, T. Zillio, E. Conlisk, and A. B. Smith, *Ecology* **89**, 2700 (2008).
- [59] R. C. Dewar and A. Porté, *J. Theor. Biol.* **251**, 389 (2008).
- [60] M. Favretti, *Entropy* **20**, 11 (2018).
- [61] S. Sibisi, J. Skilling, R. G. Brereton, E. D. Laue, and J. Staunton, *Nature (Lond)* **311**, 446 (1984).
- [62] J. C. Hoch, M. W. Maciejewski, M. Mobli, A. D. Schuyler, and A. S. Stern, *Acc. Chem. Res.* **47**, 708 (2014).
- [63] R. Kitaura, S. Kitagawa, Y. Kubota, T. C. Kobayashi, K. Kindo, Y. Mita, A. Matsuo, M. Kobayashi, H.-C. Chang, T. C. Ozawa *et al.*, *Science* **298**, 2358 (2002).
- [64] C. W. Andersen, M. Bremholm, P. N. R. Vennestrøm, A. B. Blichfeld, L. F. Lundegaard, and B. B. Iversen, *IUCrJ* **1**, 382 (2014).
- [65] A. Ferrige, M. Seddon, S. Jarvis, J. Skilling, and J. Welch, in *Maximum Entropy and Bayesian Methods* (Springer, Berlin, 1992), pp. 327–335.
- [66] K. Kimoto, T. Asaka, X. Yu, T. Nagai, Y. Matsui, and K. Ishizuka, *Ultramicroscopy* **110**, 778 (2010).
- [67] E. Scharfenaker and J. Yang, *Eur. Phys. J.: Spec. Top.* **229**, 1577 (2020).
- [68] E. Schneidman, M. J. Berry II, R. Segev, and W. Bialek, *Nature (Lond.)* **440**, 1007 (2006).
- [69] A. Tang, D. Jackson, J. Hobbs, W. Chen, J. L. Smith, H. Patel, A. Prieto, D. Petrusca, M. I. Grivich, A. Sher *et al.*, *J. Neurosci.* **28**, 505 (2008).

- [70] E. Granot-Atedgi, G. Tkačik, R. Segev, and E. Schneidman, *PLoS Comput. Biol.* **9**, e1002922 (2013).
- [71] T. Watanabe, S. Hirose, H. Wada, Y. Imai, T. Machida, I. Shirouzu, S. Konishi, Y. Miyashita, and N. Masuda, *Nat. Commun.* **4**, 1370 (2013).
- [72] R. Barrett, M. Ansari, G. Ghoshal, and A. D. White, *arXiv:2104.09668* (2021).
- [73] A. Vespignani, H. Tian, C. Dye, J. O. Lloyd-Smith, R. M. Eggo, M. Shrestha, S. V. Scarpino, B. Gutierrez, M. U. Kraemer, J. Wu *et al.*, *Nat. Rev. Phys.* **2**, 279 (2020).
- [74] D. C. G. Law, K. T. Bernstein, M. L. Serre, C. M. Schumacher, P. A. Leone, J. M. Zenilman, W. C. Miller, and A. M. Rompalo, *Ann. Epidemiol.* **16**, 797 (2006).
- [75] J. R. Artalejo and M. Lopez-Herrero, *Theor. Popul. Biol.* **80**, 256 (2011).
- [76] N. Harding, R. E. Spinney, and M. Prokopenko, *Sci. Rep.* **10**, 7646 (2020).
- [77] I. Hanski, *Nature (Lond.)* **396**, 41 (1998).
- [78] F. Ball, T. Britton, T. House, V. Isham, D. Mollison, L. Pellis, and G. S. Tomba, *Epidemics* **10**, 63 (2015).
- [79] A. Hagberg, P. Swart, and D. S. Chult, Exploring network structure, dynamics, and function using networkx, Technical Report No. LA-UR-08-05495, Los Alamos National Laboratory, Los Alamos, NM (2008).
- [80] B. Roux and J. Weare, *J. Chem. Phys.* **138**, 084107 (2013).
- [81] J. W. Pitera and J. D. Chodera, *J. Chem. Theory Comput.* **8**, 3445 (2012).
- [82] A. Cesari, A. Gil-Ley, and G. Bussi, *J. Chem. Theory Comput.* **12**, 6192 (2016).
- [83] B. Grenfell and J. Harwood, *Trends Ecol. Evol.* **12**, 395 (1997).
- [84] D. J. Watts, R. Muhamad, D. C. Medina, and P. S. Dodds, *Proc. Natl. Acad. Sci. USA* **102**, 11157 (2005).
- [85] V. Colizza, R. Pastor-Satorras, and A. Vespignani, *Nat. Phys.* **3**, 276 (2007).
- [86] P. Zhou, X.-L. Yang, X.-G. Wang, B. Hu, L. Zhang, W. Zhang, H.-R. Si, Y. Zhu, B. Li, C.-L. Huang *et al.*, *Nature (Lond.)* **579**, 270 (2020).
- [87] F. Wu, S. Zhao, B. Yu, Y.-M. Chen, W. Wang, Z.-G. Song, Y. Hu, Z.-W. Tao, J.-H. Tian, Y.-Y. Pei *et al.*, *Nature (Lond.)* **579**, 265 (2020).
- [88] P. G. Fennell, S. Melnik, and J. P. Gleeson, *Phys. Rev. E* **94**, 052125 (2016).
- [89] J. Gómez-Gardeñes, D. Soriano-Paños, and A. Arenas, *Nat. Phys.* **14**, 391 (2018).
- [90] A. Arenas, W. Cota, J. Gómez-Gardeñes, S. Gómez, C. Granell, J. T. Matamalas, D. Soriano-Paños, and B. Steinegger, *Phys. Rev. X* **10**, 041055 (2020).
- [91] H. Lau, T. Khosrawipour, P. Kocbach, H. Ichii, J. Bania, and V. Khosrawipour, *Pulmonology* **27**, 110 (2021).
- [92] D. P. Kingma and J. Ba, *arXiv:1412.6980* (2014).
- [93] See Supplemental Material at <http://link.aps.org/supplemental/10.1103/PhysRevE.106.014306> which includes a table and four figures.
- [94] Census mobility data, <https://lehd.ces.census.gov/data/lodes/LODES7/>.
- [95] D. W. Stroock and S. S. Varadhan, *Multidimensional Diffusion Processes* (Springer, Berlin, 2007).
- [96] R. Pastor-Satorras, C. Castellano, P. Van Mieghem, and A. Vespignani, *Rev. Mod. Phys.* **87**, 925 (2015).
- [97] D. Centola and M. Macy, *Am. J. Sociol.* **113**, 702 (2007).
- [98] A. Baronchelli, *R. Soc. Open Sci.* **5**, 172189 (2018).
- [99] Y. Wang, S. Wen, Y. Xiang, and W. Zhou, *IEEE Commun. Surv. Tutor.* **16**, 942 (2013).
- [100] B. K. Mishra and N. Keshri, *Appl. Math. Model.* **37**, 4103 (2013).
- [101] <https://github.com/ur-whitelab/maxent>.
- [102] <https://github.com/ur-whitelab/py0>.
- [103] D. Shah and T. Zaman, *IEEE Trans. Inf. Theory* **57**, 5163 (2011).